Int. J. Electrochem. Sci., 11 **(2016)** 6432 – 6442, doi: 10.20964/2016.08.55

International Journal of ELECTROCHEMICAL SCIENCE
www.electrochemsci.org

Synthesis and Characterization of Maghemite as an Anode for Lithium-Ion Batteries

M. Golmohammad[1,2,*], *F. Golestanifard*[1], *A. Mirhabibi*[1,3]

[1] School of Metallurgy and Materials Engineering, Iran University of Science and Technology (IUST), Tehran, Iran
[2] Faculty of Applied Sciences, Delft University of Technology, Delft, Netherlands
[3] Institute for Materials Research (IMR), University of Leeds, Leeds, United Kingdom
[*]E-mail: m_golmohammad@iust.ac.ir

Received: 9 April 2016 / *Accepted:* 12 June 2016 / *Published:* 7 July 2016

Thermal decomposition method were used to synthesize magnetite nanoparticles which then oxidized to maghemite. Simultaneous thermal analysis, X-ray diffraction, and Fourier transform infrared spectroscopy disclosed the formation of iron-urea complex and also revealed pathway of iron oxide formation from iron-urea complex in thermal decomposition method. It was demonstrated that the iron-urea complex calcined at 450°C in argon resulted in the formation of magnetite. The magnetite were heated at 230°C for 2h to be oxidized to maghemite. The formation of maghemite were confirmed using Mössbauer spectroscopy. The average particle size of obtained maghemite was estimated 43nm using field emission scanning electron microscopy and high-resolution transmission electron microscopy. The anode body was doctor bladed using maghemite with carbon black and polyvinylidene difluoride powder. Electrochemical performance of this anode in lithium-ion battery was further investigated by cyclic voltammetry and galvanostatic charge–discharge. Galvanostatic charge–discharge cycling at current density of 50 mA g^{-1} showed a reversible capacity of 538 mAh g^{-1}. The reason for this competent performance was thought to be dependent upon the size of particles.

Keywords: Maghemite; lithium-ion battery; anode; thermal decomposition; nanoparticles

1. INTRODUCTION

In recent years, one of the best choices for portable energy storage is lithium-ion batteries because of its high energy and power density [1]. However, the electrode material employed is still the main hurdle to improve lithium-ion battery performance[2], [3]. Electrode materials should have high capacity and stability as well as being inexpensive and nontoxic[1], [4]. Poizot et al. introduced transition metal oxides as an electrode material candidate for the first time in 2000 [5]. Since then,

different transition metal oxide were used as an electrode for lithium-ion battery. High capacity, low price and availability of iron oxides made them a good candidate for lithium-ion battery electrodes among transition metal oxide[6]–[14]. This high capacity of iron oxides is attributed to the reversible reaction between lithium ions (Li^+) and iron oxides (Fe_xO_y), as shown by Eq. (1).

$$Fe_xO_y + 2yLi^+ + 2ye^- \leftrightarrow xFe + yLi_2O \quad (1)$$

Among different kinds of iron oxides, magnetite (Fe_3O_4) [9]–[11], hematite (α-Fe_2O_3) [7], [8], [13], and maghemite (γ-Fe_2O_3) [12], [14], [15] have been studied as an electrode. However, the main shortcomings are low initial coulombic efficiency and capacity fading during charge-discharge which are due to the drastic volume change during the charge-discharge process and low electrical conductivity. Usage of monodisperse nano-particles can improve iron oxide performances as lithium-ion battery electrode.

There are different methods to synthesize nano iron oxides including: microemultion[16], hydrothermal[17], co-precipitation [12], [18], and thermal decomposition [19]–[22]. Amongst these methods, thermal decomposition declared promising ability for synthesis monodisperse nano-particles iron oxides. Using pentacarbonyl iron ($Fe(CO)_5$) with different surfactants, monodisperse nano-maghemite were synthesized[19], [21]. However, in these researches toxic and volatile raw material were used. Herein, we used a thermal decomposition method to synthesis nano magnetite which then was transformed to maghemite with thermal oxidation.

Different nanostructures of magnetite, maghemite, and hematite have been synthesized to boost their electrochemical properties. However, most of these methods use multi-step and complicated processes to synthesize iron oxide. In our previous study[20], we showed that thermal decomposition of iron-urea complex in air results in coexistence of hematite and maghemite in synthesized powder. In this work, maghemite was synthesized with oxidation of derived magnetite from thermal decomposition of iron-urea complex in argon. Moreover, nano-sized maghemite as an anode for lithium-ion battery were investigated.

2. EXPERIMENTAL PROCEDURE

2.1. Materials and methods

In the synthesis process, Iron (III) nitrate nonahydrate ($Fe(NO_3)_3.9H_2O$, Sigma-Aldrich) and urea ($C_3H_4N_2O$, Sigma-Aldrich) were solved in ethanol at 1:6.2 molar ratio at room temperature and stirred for 30min until a green powder were precipitated. These green precipitates were filtered and washed with ethanol several times. The obtained powders were dried at 60°C for 1h (pristine powder). To synthesize iron oxide, the pristine powder was heated at 200 and 450°C in argon for 1h which was labeled as T200 and T450, respectively. Finally, T450 was oxidized in air at 230°C for 2h to prepare maghemite.

The electrode was prepared by mixing maghemite powder with polyvinylidene difluoride powder (PVdF - Solef) and carbon black in a weight ratio of 8:3:2 in N-methyl pyrrolidone (NMP - Merk-Schuchardt) as dissolving solvent. After mixing for 30 min, homogeneous slurry was doctor

bladed on a copper foil as current collector with a thickness of 150μm and dried at 110°C. Afterward, circular disks (14mm in diameter) were punched out which then used as the test electrodes. For reference and counter electrode, metallic lithium disks and for electrolyte, 1M $LiPF_6$ dissolved in dimethyl carbonate (DMC) and ethylene carbonate (EC) (1:2 by wt. – Mitsubishi Chemicals) were used. A CR2320 coin cells (Hohsen) were used to stack these electrodes in an argon-filled glove-box (MBraun).

2.2. Characterization

The powder crystallographic structure was studied employing X-ray powder diffraction (XRD) measurements (Bruker,AXS D8 Advance) with Co-K_α radiation. High resolution transmission electron microscope (HR-TEM, Philips EM201C) and field emission scanning electron microscope (FE-SEM, TSCAN) were used to record the size and morphology of the maghemite. Thermal behavior of pristine sample were inestigated using simultaneous thermal analysis (STA) instrument (A503). Perking-Elmer Spectrum 100 was employed to record Fourier transform infrared spectroscopy (FTIR). Mössbauer spectroscopy was used to detect the iron state by using a Mössbauer SM 1201 spectrometer at room temperature with a $^{57}Co/Rh$ source in a constant acceleration transmission spectroscopy. To monitor capacity and cycling performance, galvanostatic tests with voltage limits of 0.01 and 3V vs Li/Li^+ were used employing a Maccor cycler (S-4000). Cyclic voltammetry test was carried out with an Autolab (Ecochemie) between 0.02V and 3.0V, at 0.1mV s^{-1} scan rate.

3. RESULT AND DISCUSSION

Figure 1 shows the STA pattern of pristine powder. There is a total weight loss of about 86% in two distinctive transitions between room temperature and 600°C in thermogravimetric (TG) curve.

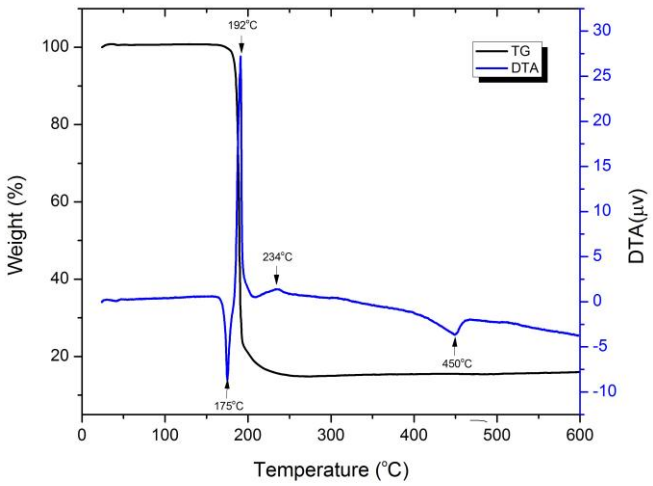

Figure 1. STA result of pristine powder in argon with heating rate of 5°C/min

The first endothermic peak in differential thermal analysis (DTA) curve at 175°C with no corresponding peak in TG curve is because of the melting of iron-urea complex. First weight loss was 78% between 185-197°C in agreement with a sharp exothermic peak in the DTA curve at 192°C. This exothermic peak is because of iron urea complex decomposition and formation of iron oxide. The second weigh lost is 8% between 205-250°C in accordance with an exothermic peak at 234°C which is attributable to the residual components burning.

Another endothermic peak at 450°C seems to be attributed to the transformation of residual Fe_2O_3 to Fe_3O_4. The transformation of hematite in H_2 is exothermic while this reaction is endothermic in argon atmosphere. For better understanding of this phenomenon, pristine powder was heated at 200°C (T200) and 450°C (T450) in argon for 1h.

Figure 2 shows XRD pattern of T200 sample which is in good agreement with the JCPDS file (Fe_3O_4, No. 19-0629) of magnetite and hematite (α- Fe_2O_3, JCPDS No. 33-0664) while T450 sample pattern confirm formation of magnetite. These patterns are in good correspondence with STA result. It can be seen that with heating at 450°C in argon, hematite phase eliminated and magnetite derived as a single phase. T200 and T450 samples showed 14±0.2 and 21±0.3 nm, respectively, calculated by the Debye-Scherrer equation.

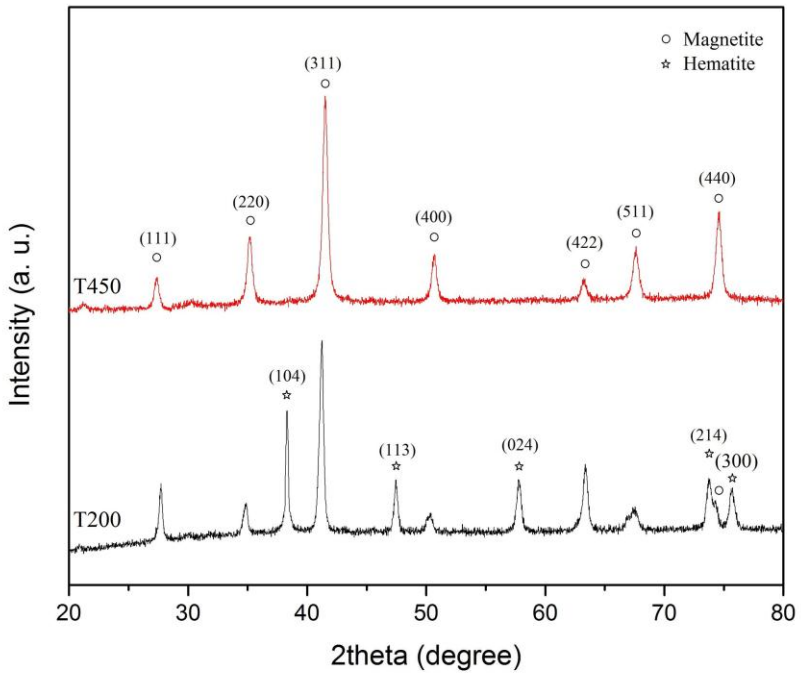

Figure 2. XRD pattern of T200 and T450 samples

XRD pattern of T200 sample is in good agreement with our previous result [20]. Heating iron-urea complex at 200°C in air or argon leads to the formation of hematite as a second phase. However, the XRD result showed heating pristine sample in argon at higher temperature (450°C) would lead to the transformation of Fe_2O_3 to Fe_3O_4 due to the oxygen deficiency. For preparing maghemite as a

single phase, T450 sample were heated at 230°C in air for 2h. The XRD pattern of maghemite sample is shown in Fig.3.

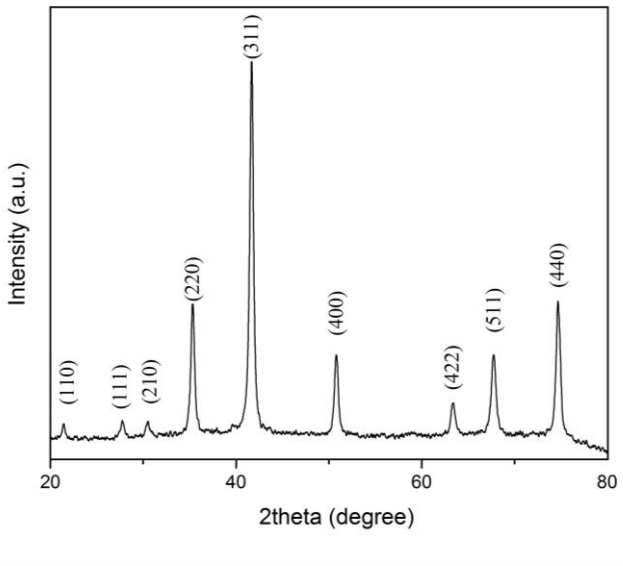

Figure 3. XRD pattern of maghemite sample

As can be seen in Fig. 3, the recorded XRD pattern of this sample agrees well with the JCPDS file (γ-Fe_2O_3, No. 39-1346) of maghemite. The crystallite size is calculated as 22±0.3 nm which declares there is not much of crystallite growth during oxidation of magnetite to maghemite. As it is widely known, distinguishing maghemite from magnetite with only XRD patterns is not trustworthy. Therefore, Mössbauer spectroscopy was performed on maghemite sample and the spectrum is presented in Fig. 4.

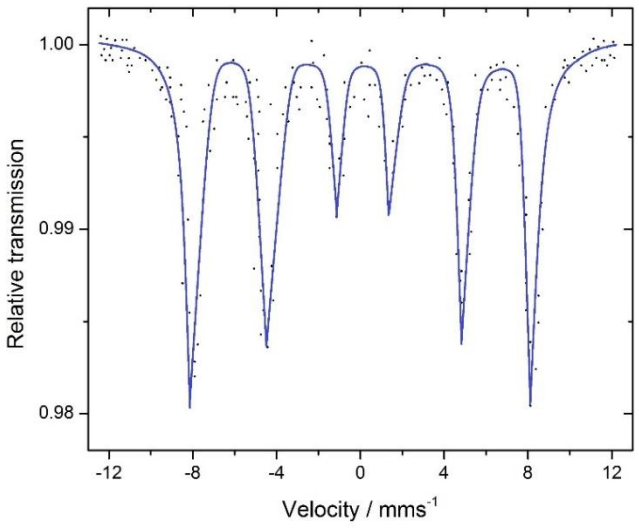

Figure 4. Mössbauer spectroscopy of maghemite sample

Mössbauer spectrum shows a sextet with approximately values of δ = 0.34 mm s^{-1} for the isomer shift, a quadrupole shift of QS=0.01 mm s^{-1}, and a hyperfine field value of B_{hf}= 49.7 T. These values are in good correspondence with maghemite data[23], [24] and show no traces of divalent iron, which confirm formation of maghemite as a single phase.

For better understanding of iron oxide formation and reaction mechanism, the FTIR test were carried out which is shown in Fig. 5. In the infrared spectra of Urea and T250, the following three changes were observed: (1) shifting of the C–O stretching vibration band from 1676 cm^{-1} to 1622 cm^{-1}, (2) shift of the C–N stretching vibration band from 1462 cm^{-1} to 1493 cm^{-1}, and finally, (3) a new strong band at 1385 cm^{-1}, which is a distinctive absorption band of NO_3^-. Increase of the C–N stretching frequency and an decrease in the C–O stretching frequency indicate that the metal ion is coordinated to urea through oxygen atoms [22].

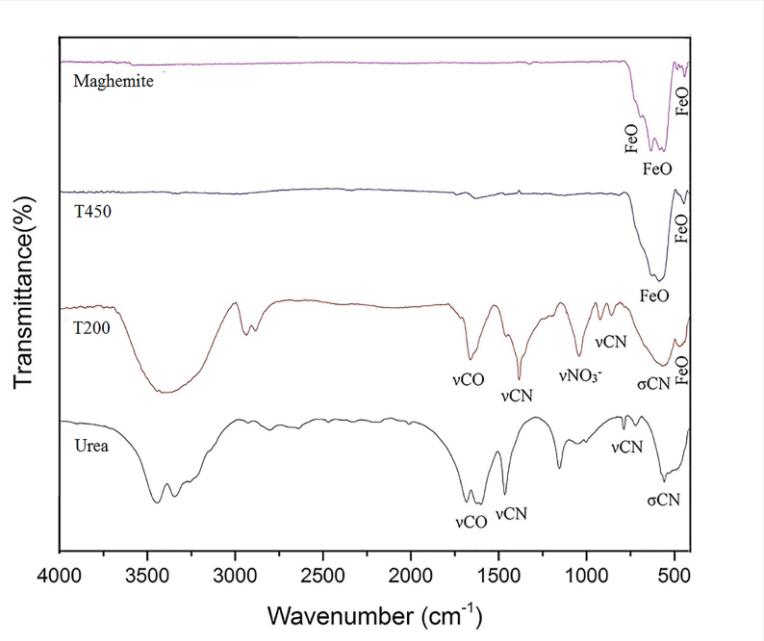

Figure 5. The FTIR result of Urea, T200, T450 and maghemite

For sample T450, there is three bands at 445, 584, and 628 cm^{-1} which are attributable to magnetite[25], while maghemite sample shows five bands at 442, 559, 638, 695, and 724 cm^{-1} which agrees well with maghemite FTIR bands[25]. Regarding our previous study [20] and the results of STA, XRD, and FTIR, heating iron-urea complex in argon leads at first to the melting of iron-urea complex and simultaneously releasing of nitrate urea and NO_2. The following reactions can be concluded from these results:

$$Fe^{3+} + 6CON_2H_4 + 3NO_3^- \leftrightarrow [Fe(CON_2H_4)_6](NO_3)_3 \quad (2)$$

$$[Fe(CON_2H_4)_6](NO_3)_3 \rightarrow [Fe(CON_2H_4)_6](NO_3)_{3-x} \quad (3)$$

$$[Fe(CON_2H_4)_6](NO_3)_{3-x} \xrightarrow{Ar} (Fe^{3+}, Fe^{2+}) + (NO_3{}^-)_{3-x} + 6CON_2H_4 \quad (4)$$

$$(Fe^{3+}, Fe^{2+}) + xOH^- \xrightarrow{Ar} Fe(OH)_x \xrightarrow{Ar} Fe_2O_3 + Fe_3O_4 + H_2O \quad (5)$$

On the other hand, the thermal decomposition product medium partially reduces iron ions, which leads to the formation of iron hydroxides. In the next stage, iron hydroxide would be transformed to iron oxide.

Figure 6 shows that maghemite sample particles are agglomerated due to heating and combustion of iron urea complex. The average size of maghemite powder is approximately 43nm. HRTEM of this powder shows particles with different size and no defined shape. Two single crystallites of this powder observed by HRTEM, showed 0.252 and 0.161 nm interplanar spacing which corresponds to {311} and{511} plane, respectively. These values for interplanar spacing match maghemite which are in good correspondence with previous results.

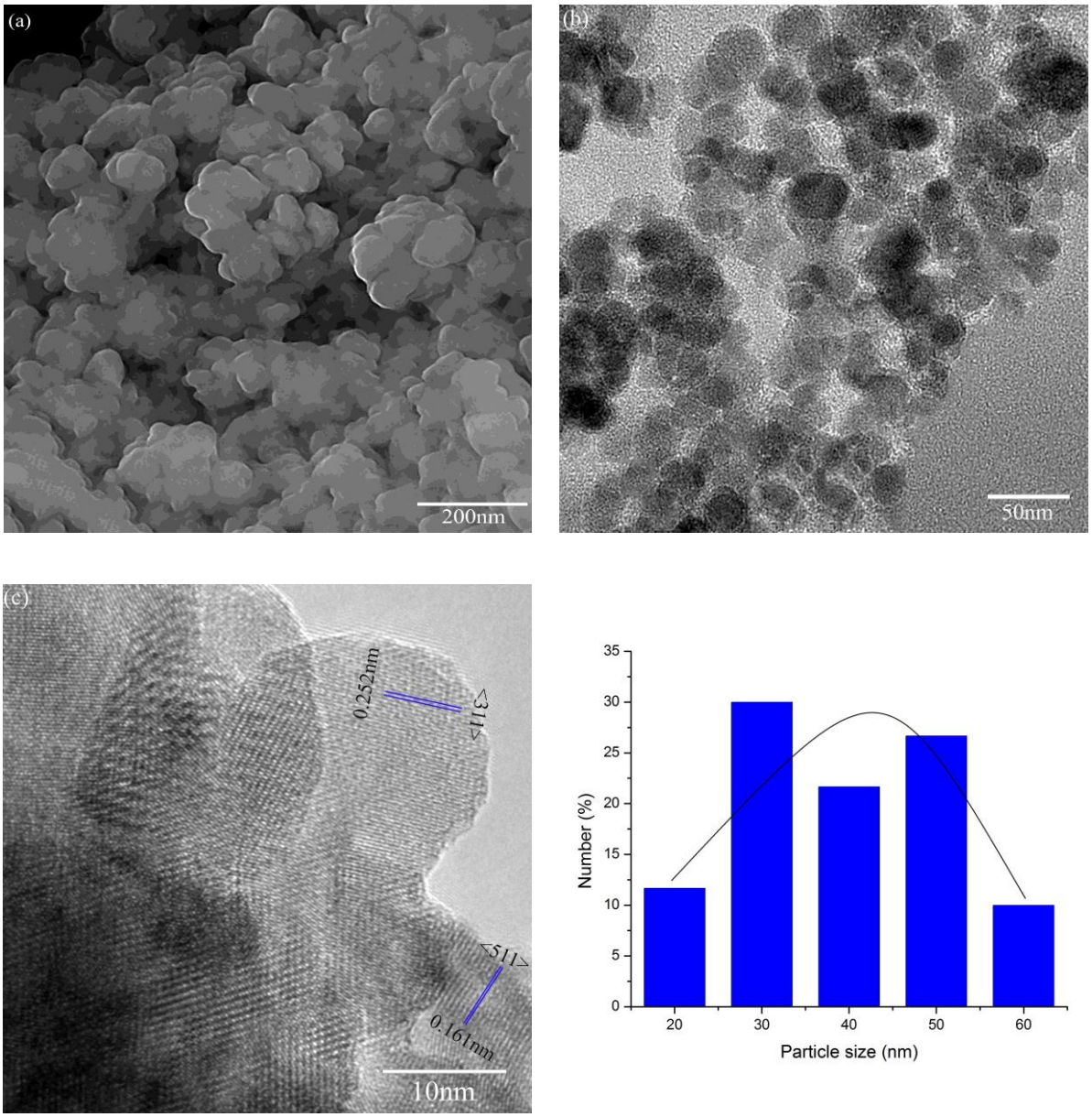

Figure 6. Morphology of the maghemite sample (a) FESEM, (b) TEM, c) HR-TEM, (d) histogram

The electrochemical behavior of the anode were studied employing galvanostatic charge-discharge at 50 mAg^{-1} current density and cyclic voltammetry (CV) at 0.1 mV s^{-1} scanning rate which has been shown in Fig. 7 and Fig. 8, respectively. For the first discharge cycle three distinctive features can be observed (Fig. 7 (a)). A small plateau at about 1.6V refers to the lithium ions intercalation into the maghemite structure which results in the formation of a Li–Fe–O complex (Eq. (6)). Voltage drop to about 0.8 V, shows another plateau which is attributable to formation of the Fe and Li_2O from the Li–Fe–O complex (Eq. (7)). The slow voltage falloff from 0.7 V to 0.01 V attributed to the formation of Solid Electrolyte Interphase (SEI) [1].

$$Fe_2O_3 + xLi = Li_xFe_2O_3 \quad (6)$$

$$Li_xFe_2O_3 + (6 - x)Li = 2Fe + 3Li_2O \quad (7)$$

Total capacity of 1284 mAh g^{-1} was delivered during the first cycle discharge for maghemite sample, while the discharge capacity after 50 cycles was about 538 mAh g^{-1}. Maghemite theoretical capacity is about 1006 mAh g^{-1} and the additional capacity in the first cycle is due to the SEI formation which is notified by other researchers as well[12], [14]. Fiftieth discharge cycle shows the first two voltage plateau while the third plateau is gone due to passivity of SEI which after the first cycle, the formation of SEI wouldn't be continued.

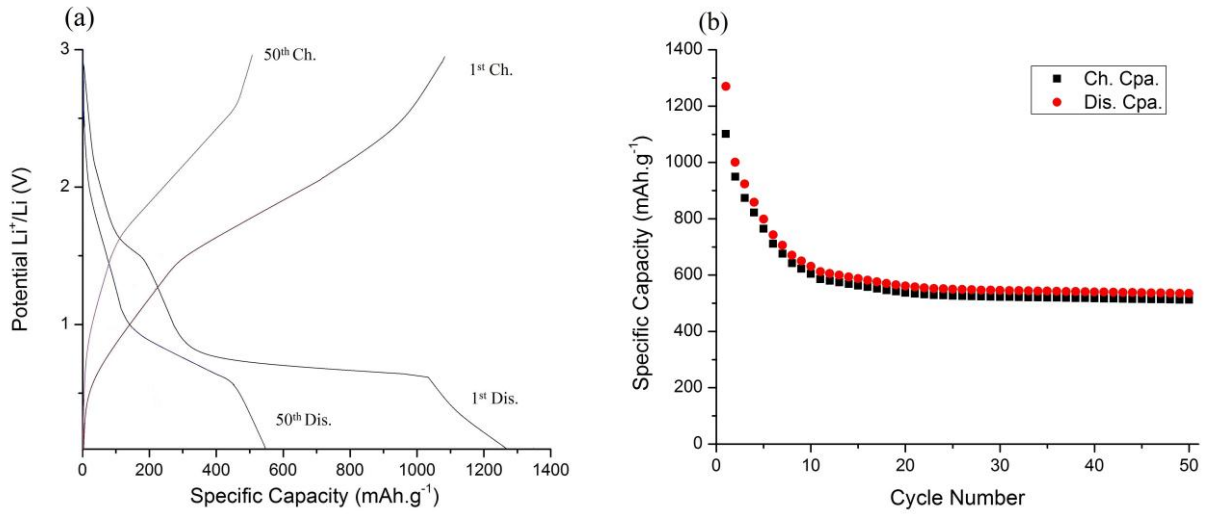

Figure 7. Electrochemical properties of maghemite sample (a) Potential Li+/Li vs. Specific capacity (b) Specific capacity Vs. Cycle number

Figure 7 (b) shows the discharge-charge capacities vs. cycle numbers for maghemite sample at a current density of 50 mA g^{-1}. The maghemite sample showed a good electrochemical performance as an anode. It showed high reversible capacity and cycleability comparing to the results of other researches[26], [27], which benefited from nanometric particle size. The capacity loss up to the 15 cycles is due to the huge volume changes during the insertion and extraction of lithium ions that results in pulverization and fragmentation of electrodes and loss of electrical contacts[26].

As can be seen in Fig. 8, there is two small reduction peaks at 1.6 and 1V in the first cycle that can be due to the lithium intercalation reaction (Eq. (6). The first peak at 1.6V is attributed to the lithium insertion into maghemite structure[28]. The second peak at 1V is due to the formation of $Li_2Fe_2O_3$ [26] which is in good correspondence with galvanostatic results. The sharp cathodic peak at around 0.67V is attributable to the reduction of Fe^{2+} to Fe^0, and the electrolyte decomposition and SEI layer formation. The anodic peak at 1.65 V is attributed to the reversible oxidation of Fe^0 to Fe^{3+}. The second cathodic curve shows a sharp reduction peak at 0.85 V which has been shifted to higher voltage due to the structure and phase evolution. As can be seen there is no sign of 1.6 and 1 V peaks which declare that the iron oxide formed in charge process is amorphous and the intermediated phases won't be formed in second cycle. The second anodic peak at 1.75 V is shifted to higher voltage due to the electrochemical polarization[29].

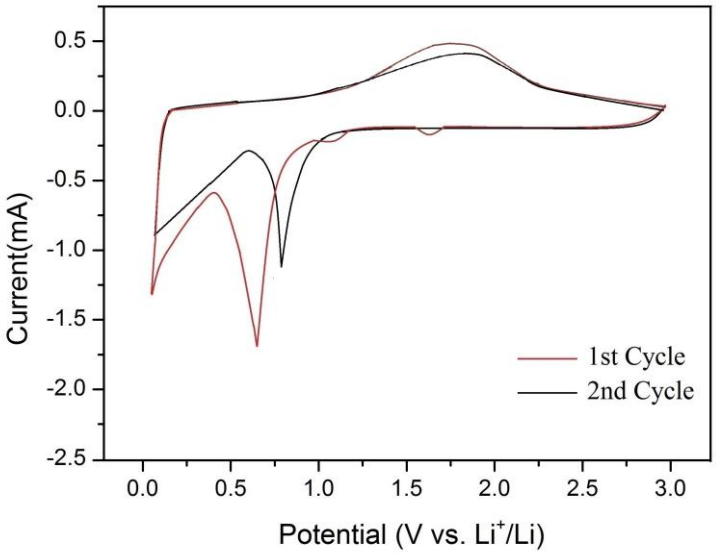

Figure 8. Cyclic voltammetry of maghemite sample at scanning rate of 0.1 mV/s

The current work showed good cyclicing performance comparing to similar cells made of iron oxides[14], [27]. These counterparts showed reversible capacity of 400[14] and 450[27] mAh g^{-1} at current density of 50 & 100 mAh g^{-1}, respectively which is less than the result of current work. The result of this research, based on a conventional anode configuration, indicate that control of nanoparticle size can improve cell performance.

4. CONCLUSION

The synthesis of magnetite nanoparticles via a simple, single-step thermal decomposition of iron-urea complex were accomplished. STA and FTIR results disclosed that heating iron-urea complex at 200°C in argon leads to removal of urea and NO_2 as gaseous and iron oxide formation. . XRD result showed heating iron urea complex at 200°C in argon leads to coexistence of magnetite and hematite

while heating it at 450°C in argon would leads to the formation of magnetite as a single phase due to the oxygen depletion. Maghemite nanoparticles were prepared by oxidation of obtained magnetite. XRD and Mössbauer results confirmed formation of maghemite as a single phase and showed no trace of Fe^{2+}. FESEM and HRTEM results disclosed that derived maghemite had an average particle size of 43nm. Electrochemical characterization of the maghemite as an anode for lithium ion battery showed first capacity of ~1284 mAh g^{-1} and reversible capacity of about 538 mAh g^{-1} for charge–discharge rates of 50 mAh.g^{-1}. Moreover, CV results disclosed the pathway of lithium reaction with maghemite and showed iron oxide formed in first charge cycle lose the ability of lithium ions accommodation in its structure. The good cyclability and capacity retention of the anode is the result of nananometric size of the maghemite particles.

References

1. N. Nitta, F. Wu, J. T. Lee, and G. Yushin, *Mater. Today*, 18 (2015) 252.
2. B. L. Ellis, K. Town, and L. F. Nazar, *Electrochim. Acta*, 84 (2012) 145.
3. J. Chen, *Materials (Basel)*, 6 (2013), 156.
4. M. Armand and J.-M. Tarascon, *Nature*, 451 (2008), 652.
5. P. Poizot, S. Laruelle, S. Grugeon, L. Dupont, and J. M. Tarascon, *Nature*, 407 (2000) 496.
6. M. Valvo, E. García-Tamayo, U. Lafont, and E. M. Kelder, *J. Power Sources*, 196 (2011) 10191.
7. P. Tartaj, M. a D. P. Morales, S. Veintemillas-Verdaguer, T. Gonz lez-Carre o, and C. J. Serna, *J. Phys. D. Appl. Phys.*, 36 (2003) R182.
8. Y. Sun, J. Zhang, T. Huang, Zh, Liu, A. Yu, *Int. J. Electrochem. Sci.* 8 (2013) 2918.
9. M. E. Im, D. Pham-Cong, J. Y. Kim, H. S. Choi, J. H. Kim, J. P. Kim, J. Kim, S. Y. Jeong, and C. R. Cho, *J. Power Sources*, 284 (2015) 392.
10. M.-Y. Li, Y. Wang, C.-L. Liu, H. Gao, and W.-S. Dong, *Electrochim. Acta*, 67 (2012) 187.
11. M. Zheng, D. Qiu, B. Zhao, L. Ma, X. Wang, Z. Lin, L. Pan, Y. Zheng, and Y. Shi, *RSC Adv.*, 3 (2013) 699.
12. M. Golmohammad, A. Mirhabibi, F. Golestanifard, and E. M. Kelder, *J. Electron. Mater.*, 45 (2016) 426.
13. H. Morimoto, S. Tobishima, and Y. Iizuka, *J. Power Sources*, 146 (2005) 315.
14. Y. Wu, P. Zhu, and M. Reddy, *ACS Appl. Mater. Interfaces*, 6 (2014) 1951.
15. M. Golmohammad, F. Golestanifard, and A. Mirhabibi, and E. M. Kelder, *Ceram. Int.*, 42 (2016) 4370.
16. J. Vidal-Vidal, J. Rivas, and M. a. López-Quintela, *Colloids Surfaces A Physicochem. Eng. Asp.*, 288 (2006) 44.
17. O. Horner, S. Neveu, S. Montredon, J.-M. Siaugue, and V. Cabuil, *J. Nanoparticle Res.*, 11 (2009) 1247.
18. A. Lak, F. Ludwig, J. M. Scholtyssek, J. Dieckhoff, K. Fiege, and M. Schilling, *IEEE Trans. Magn.*, 49 (2013) 201.
19. S. Sun and H. Zeng, *J. Am. Chem. Soc.*, 124 (2002) 8204.
20. M. Golmohammad, F. Golestanifard, and A. Mirhabibi, *J. Adv. Mater. Process.*, 3 (2015) 26.
21. T. Hyeon, S. S. Lee, J. Park, Y. Chung, and H. B. Na, *J. Am. Chem. Soc.*, 123 (2001), 12798.
22. O. Carp, L. Patron, L. Diamandescu, and A. Reller, *Thermochim. Acta*, 390 (2002) 169.
23. C. Cannas, a. Ardu, D. Niznansky, D. Peddis, G. Piccaluga, and a. Musinu, *J. Sol-Gel Sci. Technol.*, 60 (2011) 266.

24. A. Lak, J. Dieckhoff, F. Ludwig, J. M. Scholtyssek, O. Goldmann, H. Lünsdorf, D. Eberbeck, A. Kornowski, M. Kraken, F. J. Litterst, K. Fiege, P. Mischnick, and M. Schilling, *Nanoscale*, 5 (2013) 11447.
25. M. Gotić, G. Koščec, and S. Musić, *J. Mol. Struct*., 924–926 (2009) 347.
26. D. Larcher, C. Masquelier, D. Bonnin, Y. Chabre, V. Masson, J.-B. Leriche, and J.-M. Tarascon, *J. Electrochem. Soc*., 150 (2003), A133.
27. O. Vargas, Á. Caballero, and J. Morales, *Electrochim. Acta*, 130 (2014), 551.
28. A. Abbasi, A. Mirhabibi, H. Arabi, M. Golmohammad, and R. Brydson, *J. Mater. Sci. Mater. Electron*., (2016) http://dx.doi.org/10.1007/s10854-016-4788-7.
29. S.-H. Yu, D. E. Conte, S. Baek, D.-C. Lee, S.-K. Park, K. J. Lee, Y. Piao, Y.-E. Sung, and N. Pinna, *Adv. Funct. Mater*., 23 (2013) 4293.